PAPER

Check for updates

Tracing proton conduction pathways in polycrystalline MOF-based core–shell systems†

Damian Jędrzejowski, [ID] ‡[ab] Marzena Pander, [ID] ‡[ac] Emilian Stachura, [ID] [c] Krzysztof Matlak, [ID] [d] Wojciech Bury [ID] *[c] and Dariusz Matoga [ID] *[a]

Metal–organic frameworks (MOFs) have emerged as proton conductors, however, understanding conduction mechanisms and pathways in MOFs is limited by the common polycrystalline form of these materials, resulting in the presence of grain boundaries. Herein, we report model core–shell systems based on the UiO-68 platform with incorporated tetrazine function for studying proton conduction in polycrystalline MOFs. The solvent-assisted linker exchange (SALE) method, applied to two model MOFs of the UiO-68 family, enables core shell swapping, control over the degree of linker exchange, and stability of the system. The subsequent use of the inverse electron-demand Diels–Alder (iEDDA) reaction with an acid dienophile precisely in the core or shell of microcrystals, followed by encapsulation of imidazole (HIm), resulted in the formation of a diverse group of polycrystalline proton-conducting systems differing in the distribution of pendant carboxylic groups and concentration of imidazole charge carriers. Comprehensive impedance studies of these covalently modified model systems revealed minor differences between their proton conductivity values, and considerable differences between activation energies, and pseudocapacitances. These unprecedented observations demonstrate the significant role of external surface conduction in polycrystalline MOFs.

Introduction

Metal–Organic Frameworks (MOFs) have emerged as a versatile class of porous materials[1] that can be tailored for specific functions using principles of reticular synthesis.[2] Among numerous applications of MOFs, of particular interest is their use as solid-state proton conductors for constructing proton exchange membrane fuel cells (PEMFCs).[3] In this case, a key advantage of MOFs is their tunable porosity and chemical functionalization, which can significantly enhance the mobility and concentration of charge carriers.[4] This functionalization involves introducing Brønsted acid groups prior to MOF assembly[5] or post-synthetically by placing them directly on the backbone[6] or in guest molecules.[7] On the other hand, the crystallinity of MOFs enables the study of conduction phenomena using relatively simple structural and theoretical

models, which is often practically impossible for non-crystalline polymer conductors.[8,9] Overall, however, despite the substantial body of literature demonstrating the successful use of MOFs as proton conductors, one issue that remains largely
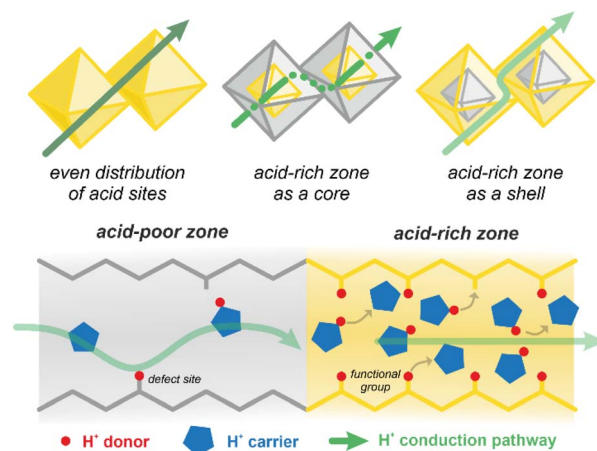

Fig. 1 (Top) Schematic representation of the effect of the distribution of acid-rich and acid-poor zones on macroscopic proton conduction in polycrystalline core–shell MOFs. The arrows represent the favored possible conduction pathways; (Bottom) schematic representation of the effect of the concentration of proton donors (red dots) and proton carriers (blue pentagons) on the dominant conduction mechanism in the two zones.

aFaculty of Chemistry, Jagiellonian University, Gronostajowa 2, Kraków 30-387, Poland. E-mail: dariusz.matoga@uj.edu.pl

bDoctoral School of Exact and Natural Sciences, Jagiellonian University, Łojasiewicza 11, Kraków 30-348, Poland

cFaculty of Chemistry, University of Wrocław, F. Joliot-Curie 14, Wrocław 50-383, Poland. E-mail: wojciech.bury@uwr.edu.pl

dNational Synchrotron Radiation Centre SOLARIS, Czerwone Maki 98, Kraków 30-392, Poland

‡ These authors contributed equally to this work.

This journal is © The Royal Society of Chemistry 2025

J. Mater. Chem. A, 2025, **13**, 23671–23679 | **23671**

underexplored is inter-grain conduction in polycrystalline samples (Fig. 1). Although electrochemical impedance spectroscopy (EIS) can help identify the dominant conduction pathway, whether it is intra-grain, inter-grain, or intermediate, such as surface conduction, it is extremely difficult to isolate these pathways experimentally on a macroscopic scale.[10,11]

We hypothesized that the study of proton conduction pathways in polycrystalline samples may be possible with materials that offer precise control over crystal structure and composition. In this context, we planned to synthesize a pair of core–shell and reverse core–shell MOFs with corresponding reference core-only and shell-only compounds as a model for such studies. In general, core–shell MOFs are specific representatives of the so-called 4th generation of MOFs[12] or hierarchical systems, which can exhibit enhanced properties such as stability,[13] processability,[14] and synergistic effects in specific applications.[15,16] Such hierarchical structures have already been demonstrated in multivariate MOFs (MTV-MOFs)[17–19] with regularity on molecular[20] or domain[21] scales, and in MOF-X composites, where X may represent polymers,[22] carbons,[23] metal oxides,[24] or other MOFs (in MOF–MOF systems).[25–27] In this view, core–shell MOFs, as a specific category of MTV-MOFs, are typically obtained either through the epitaxial growth of a shell-MOF on a pre-synthesized core-MOF,[28] or via solvent-assisted linker exchange, SALE (also known as post-synthetic exchange (PSE) of linkers).[29] The latter approach is often limited to building blocks with similar structural parameters and relies on diffusion as a rate-limiting step.[30,31] However, although core–shell MOFs have been explored extensively recently, such systems have never been used to study proton conduction before (Fig. 1).

In this work, to study proton conduction in polycrystalline MOF samples, we employed model core–shell systems based on the UiO-68(TZ) MOF (TZ = 1,2,4,5-tetrazine or s-tetrazine), which allows the introduction of acid sites in the form of carboxyl groups through covalent modification. In order to precisely control the distribution of carboxyl moieties in our core–shell MOFs, we combined the SALE method and inverse electron-demand Diels–Alder (iEDDA) reaction (Fig. 2). In addition, to make our investigations independent of the influence of humidity, our model materials were designed to exhibit good measurable conductivity under anhydrous conditions (above 100 °C), which was achieved by vapor adsorption of imidazole (HIm) proton carriers. From an application point of view (in PEMFCs), higher operating temperatures of proton conductors reduce the poisoning potential of Pt catalysts and the potential for flooding of electrodes by condensing water; improve reaction kinetics and provide an alternative to Nafion, which dehydrates above 80 °C.

Results and discussion

In this work, we selected the tetrazine-based UiO-68 analogue, denoted as UiO-68(TZ), which features Zr_6 nodes coordinated by twelve carboxylate groups from 4,4′-(1,2,4,5-tetrazine-3,6-diyl) dibenzoate linkers (TZDC, Fig. 2) as a major platform for the study. The presence of the tetrazine moiety is a key feature,[32,33]
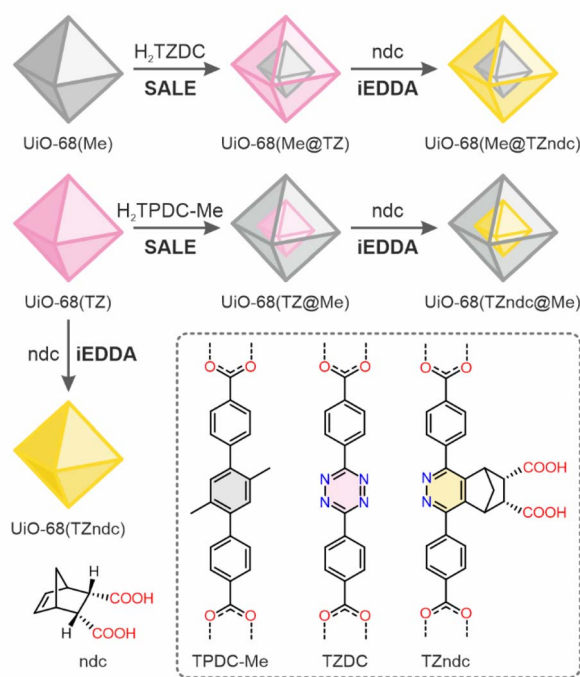

Fig. 2 Strategies of linker exchange (SALE) and covalent modification (iEDDA) for the preparation of UiO-68 type MOFs with controlled distribution of carboxyl acid sites (shown in yellow); TPDC-Me, TZDC and TZndc linkers are shown within dashed-line rectangle.

enabling the post-synthetic introduction of carboxyl groups that serve a dual function as proton donors or acceptors (when deprotonated) in the conduction pathway. While this material proved to be a promising platform for iEDDA modification, a notable limitation of UiO-68(TZ) is its decreased stability upon desolvation, which necessitates a laborious preparation process to maintain its porosity.[34] To address this challenge, we applied a straightforward strategy for the preparation of core–shell MOFs using the SALE protocol,[35] where the shell serves as a protective layer for the material. The corresponding reverse core–shell materials were prepared in an analogous way (Fig. 2) and the two dual-domain systems were used as models in proton conduction mechanistic studies.

Synthesis and characterization of phase-pure MOFs

The UiO-68(TZ) material was synthesized following optimized procedure (ESI, Section 3.2†) and confirmed to be isostructural with UiO-68,[36] exhibiting high crystallinity when soaked in DMF (Fig. 3a). However, the PXRD patterns of samples dried after solvent exchange (tested with acetone, dichloromethane, and supercritical CO_2) showed reduced crystallinity (Fig. S7†). In line with the findings of Martí-Gastaldo et al.,[34] we observed that the activation with hexane leads to improved porosity of the material, however the measured N_2 uptake remained below the theoretical value of 1140 cm^3 g^{-1} (Fig. S29a and S54a†). Further structural characterization was performed using scanning electron microscopy (SEM, Fig. S32†), nuclear magnetic resonance (NMR) and infrared (IR) spectroscopy (Fig. S15 and S22†),
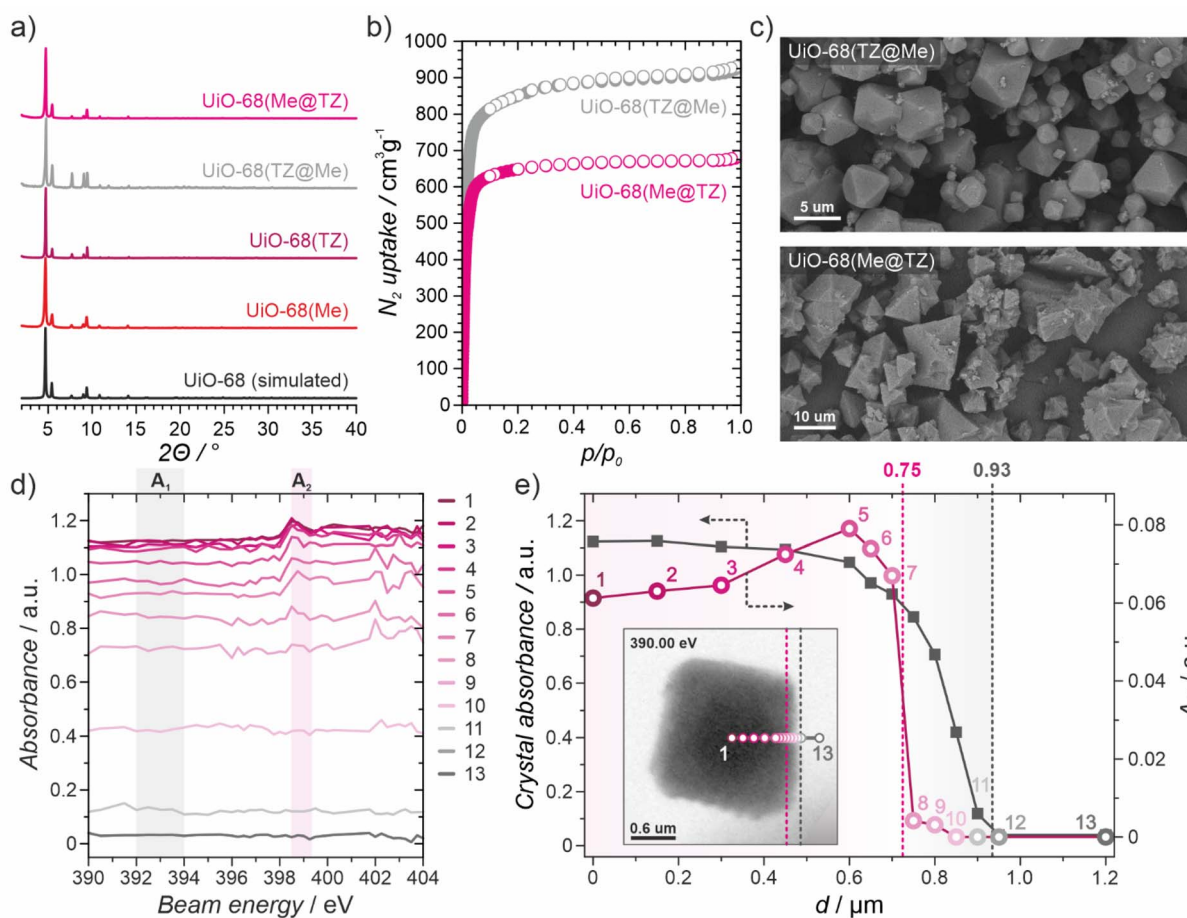
23672 | J. Mater. Chem. A, 2025, 13, 23671–23679

This journal is © The Royal Society of Chemistry 2025

Fig. 3 a) PXRD patterns of the phase-pure MOFs: UiO-68(TZ), UiO-68(Me), and derived core−shell materials: UiO-68(TZ@Me), UiO-68(Me@TZ), compared to UiO-68 (simulated). (b) N_2 sorption isotherms (at 77 K) of the core−shell materials, closed symbols (adsorption), open symbols (desorption). (c) SEM images of the core−shell materials. (d) X-ray absorption spectra of UiO-68(TZ@Me) collected along the axis from crystal center (points 1−13). Areas A_1 and A_2 marked for the calculation of A_N parameter, for nitrogen abundance estimation. For details see ESI, Section S12† (e) X-ray absorbance at 390 eV for the UiO-68(TZ@Me) crystal probed at 13 points shown in the inset, together with the calculated A_N. The limiting values of both the absorbance at 390 eV and A_N determine the crystal surface boundary (grey dashed line) and the limit of the presence of nitrogen in the crystal (pink dashed line).

and thermogravimetry (TG) analysis (Fig. S50†). SEM imaging showed octahedral crystallites with a median size of 1.15 μm (moderately homogenous size distribution), while NMR analysis confirmed the intact TZDC linker. IR analysis detected no excess of free protonated carboxylates, and TG analysis revealed reduced thermal stability, with gradual decomposition starting at 260 °C and completing at around 500 °C.

As a complementary UiO-68 analogue for our studies, we selected UiO-68(Me), also known as PCN-56,[37] that contains deprotonated H_2TPDC-Me as a linker (Fig. 2). The usage of H_2TPDC-Me instead of H_2TPDC[36] in UiO-68 offers significantly improved solubility and control over the MOF synthesis. Pure-phase UiO-68(Me) was synthesized following reported protocol (ESI, Section 3.2†).[37] Enhanced solubility of H_2TPDC-Me in DMF enabled the formation of larger crystals with improved yield and uniform size distribution, as shown in SEM images (Fig. S33†). PXRD analysis (Fig. 3a and S9†) confirmed the retention of crystallinity after a standard activation procedure (acetone exchange and drying at 80 °C). TG analysis (Fig. S50†)

demonstrated good thermal stability, with decomposition beginning at approximately 450 °C. N_2 sorption analysis at 77 K confirmed the porosity of UiO-68(Me), showing N_2 uptake of 820 cm³ g⁻¹ (Fig. S29b and Table S4†), which aligns well with theoretical values of 900 cm³ g⁻¹ (Fig. S54b†). These findings further emphasize the stability differences between UiO-68(TZ) and UiO-68(Me).

Tetrazine-based core–shell MOFs

To develop functional materials with enhanced stability, core–shell hybrids based on UiO-68(TZ) and UiO-68(Me) were prepared using the SALE strategy (Fig. 2). We adopted a consistent naming convention for these materials, which reflects their heterogeneous linker distribution. The structures are labeled in the form UiO-68(core_linker@shell_linker). For example, in UiO-68(TZ@Me), the core consists of TZDC linkers, while the shell is composed of TPDC-Me linkers. The same naming protocol applies to the iEDDA-modified materials, where the modified linker is designated as TZndc. The reaction of UiO-

This journal is © The Royal Society of Chemistry 2025

J. Mater. Chem. A, 2025, **13**, 23671–23679 | **23673**

68(TZ) with H_2TPDC-Me in DMF led to the formation of UiO-68(TZ@Me) and displayed rapid kinetics, achieving over 50% ligand exchange within 15 minutes at 60 °C (ESI, Section S3.3†). In contrast, the preparation of UiO-68(Me@TZ), based on reported protocol involving non-methylated TPDC linker,[34] required longer reaction times (4 hours at 80 °C) due to the low solubility of the H_2TZDC ligand and larger crystal size of UiO-68(Me). This procedure resulted in core–shell samples with only 25% TZDC linker exchange.

The yield of SALE in both systems was quantified via ^{1}H NMR analysis of digested samples (ESI, Fig. S16 and Section S5.5†). PXRD analysis confirmed well-preserved crystallinity and isostructural nature of both core–shell systems (Fig. 3a and S10†). SEM images (Fig. 3c, S34 and S35†) showed consistent octahedral crystallite morphologies and revealed preserved crystallite size distributions. N_2 sorption at 77 K (Fig. 3b and S30†) indicated retained porosity in UiO-68(TZ@Me), closely resembling N_2 uptake of UiO-68(Me), whereas UiO-68(Me@TZ) showed reduced porosity. TG analysis (Fig. S51†) revealed two decomposition steps for both samples: the first around 260 °C and the second above 500 °C, mirroring the thermal behavior of the phase-pure UiO-68(x) analogues studied here.

Additional SALE experiments were conducted to study the formation of UiO-68(TZ@Me) in successive cycles. NMR analysis of linkers content showed almost complete exchange of TZDC to TPDC-Me after five cycles (Fig. S17 and S20†). A decrease in exchange ratio was observed in subsequent cycles, likely due to the increasing difficulty of linker diffusion into the MOF crystal core. DRIFT analysis confirmed the presence of both linkers, with differences in band intensities in the 1480–1320 cm^{-1} region reflecting composition changes in UiO-68(TZ@Me) after each SALE cycle (Fig. S24†). PXRD (Fig. S11†) and SEM analyses (Fig. S36†) supported the retention of crystallinity and morphology. Additionally, scaling up the preparation of UiO-68(TZ@Me) with 500 mg of starting MOF yielded consistent linker composition (ESI, Section S3.3†). For UiO-68(Me@TZ), extending the reaction time increased the TZDC content to 50%; however, DRIFT spectra indicated the presence of uncoordinated H_2TZDC in the sample (Fig. S23†).

In characterizing the two hybrid materials, substantial indirect evidence supported the core–shell-like distribution of ligands in the crystallites, but direct confirmation requires advanced physicochemical methods. Since UiO-68(TZ) and UiO-68(Me) differ only in one aromatic ring structure, with no particular distinctions, basic imaging methods like SEM-EDS or Raman microscopy are insufficient. Similar challenges were addressed in the work of A. Centrone et al.,[38] where infrared nanoscopy and diffraction-limited hyperspectral photoluminescence were applied to analyze ligand distribution in core–shell materials based on UiO-68 analogues (UiO-68(TPDC@TZ) systems with tetrazine shell).

Here, we used Scanning Transmission X-ray Microscopy (STXM) with synchrotron radiation to confirm the core–shell structure in UiO-68(TZ@Me) (ESI, Section S11†). Samples were activated and measured under vacuum, focusing on the nitrogen absorption edge (398.50 eV) to trace the tetrazine core. STXM imaging was performed along the C_2 axis of the octahedral crystallites, sampling areas from the center outwards (Fig. 3e, inset). X-ray absorption spectra for 13 regions indicated a crystal boundary at 930 nm and a nitrogen-rich region extending to 750 nm, yielding a shell thickness of 180 nm for a 1.86 μm crystallite (Fig. 3e). These results closely match NMR-based shell thickness estimates (175 nm, ESI, Section S11†). Additional measurements along different axes and for other crystallites confirmed these findings (Fig. S59†). Together, these analyses validate the core–shell structure of UiO-68(TZ@Me) and demonstrate the utility of STXM for mapping ligand distributions in complex materials.

Post-synthetic modifications of tetrazine-based MOFs

Among the various functions of s-tetrazine, its role as a reactive diene in the iEDDA reaction is particularly valuable. This reaction type has garnered significant attention due to its high yields, chemoselectivity, irreversibility (when appropriate diene is used), mild conditions, and versatility.[39,40] Due to the orthogonality of the iEDDA reaction with coordination bond formation, it is theoretically possible to introduce functional groups that are difficult to incorporate via standard de novo approach or post-synthetic modification which, in general, has become an essential tool for functionalizing MOFs.[41,42] Only several applications of the iEDDA reaction in MOFs have been reported,[43–46] such as the rigidifying of flexible frameworks while preserving crystallinity,[47] the introduction of hydroxyl groups for luminescence-based humidity sensing while retaining flexibility[48] or the post-synthetic conjugation of fullerenes or carbon nanotubes on MOF surfaces.[49,50]

Here, our objective was to influence proton conduction properties by introducing groups that could act as proton donors or acceptors. To verify reactivity in a model core–shell system, UiO-68(TZ@Me), we explored three dienophiles with the following functional groups (Fig. S1†): an amine (ncn), monocarboxylic (nca), and dicarboxylic (ndc), all of them being norbornene derivatives for faster reaction kinetics (ESI, Section S3.3, Fig. S12, S18 and S25†). For better reaction control and increased proton donor concentration, ndc was selected as the primary dienophile for further study, yielding UiO-68(TZndc@Me) (Fig. 2). This reaction proceeded under mild conditions (at 60 °C for 12 h, see Section 3.3 in ESI† for details). Reaction completion was visually confirmed by color change from pink to bright yellow (Fig. S5†), while FT-IR analysis showed the disappearance of the 1380 cm^{-1} (Fig. S26†) tetrazine band, and NMR analysis of the digested sample confirmed quantitative formation of the TZndc ligand (Fig. S18†). PXRD analysis indicated that crystallinity was fully retained (Fig. S13†), and SEM images confirmed preservation of crystallite size distribution and morphology (Fig. S37†). As expected, the porosity of UiO-68(TZndc@Me) decreased ($S_{BET} = 2446$ m^2 g^{-1}; before modification 3455 m^2 g^{-1}, $V_{pore} = 1.00$ cm^3 g^{-1}; before modification 1.42 cm^3 g^{-1}, Table S4 and Fig. S31†). Despite the incorporation of relatively large side groups, the remaining voids in the unit cell volume are considerable, allowing for potential applications, such as proton carrier diffusion.

23674 | J. Mater. Chem. A, 2025, 13, 23671–23679

This journal is © The Royal Society of Chemistry 2025

To further demonstrate the versatility of our modification method and analyze the influence of free carboxyl group distribution on proton conductivity, the modifications with ndc were also performed on UiO-68(TZ) and UiO-68(Me@TZ) (Fig. 2). Each of these materials reacted similarly to UiO-68(TZ@Me), with physicochemical studies confirming modification completeness and crystallite shape and morphology preservation (ESI, Fig. S13, S26, S38 and S39†).

Proton conduction (PC) studies

The primary challenge affecting the interpretation of proton conduction in UiO-68(TZ) based materials is the influence of humidity. Our preliminary studies indicated that UiO-68(TZ) loses crystallinity at lower humidity than analogous materials, such as UiO-68(Me) (Fig. S8†). To decouple our research findings from this critical factor, our materials were prepared without the presence of water, and conduction tests were carried out under anhydrous conditions. Such measurements are essential in the search for a stable proton conductor that operates at temperatures above 100 °C without the requirement for constant hydration.[51,52]

Due to the large voids present in the investigated materials, their proton conduction is likely mediated by carriers occupying these voids. Consequently, the proton carrier should be a Brønsted base, have high mobility, and remain inert to the material itself. Based on these criteria and a literature review,[53,54] imidazole (HIm) was selected as an optimal proton carrier. We studied HIm incorporation in a series of materials with varying free carboxyl content, *i.e.* composed of UiO-68(Me) and UiO-68(TZndc) domains, with the content of the latter at 0, 25, 55 and 100%. This series underwent a standard imidazole adsorption procedure, reaching thermodynamic equilibrium under specified conditions (100 mbar, 120 °C, see ESI, Section S3.4† for details). The amount of adsorbed imidazole, determined by ^{1}H NMR analysis (Sections S5.4 and S5.6†), correlated positively with the concentration of free carboxyl groups (Fig. S21†). This observation was further corroborated with the simulated incorporation of HIm in UiO-68 type models based on the studied linkers (Fig. 2), where a higher affinity of physisorbed imidazole towards the "acid-rich" UiO-68(TZndc) material was observed (ESI, Section S10.2†). All studied materials retained crystallite size and morphology upon imidazole infiltration (Fig. S40–S43†). PXRD analysis verified the retention of the crystalline structure (Fig. S14†), except for UiO-68(TZndc), which did not maintain crystallinity during earlier stages, and confirmed the absence of extra HIm phases.

The domain structure of our Zr-MOF materials provided the opportunity for quantitative and qualitative analysis of proton conduction in polycrystalline samples due to well-defined distributions of free carboxyl groups. Carboxyl groups serve a dual role in this study: as proton donors to locally increase the concentration of H_2Im^+ carriers and as intermediates in the conduction pathway, leveraging their strong hydrogen-bonding capability.

Two imidazole-free samples (UiO-68(TZ@Me) and UiO-68(TZndc@Me)) and a series of imidazole-functionalized samples (HIm@Zr-MOF) were analyzed for anhydrous proton conduction in the 110–160 °C temperature range. Details of sample preparation and the equipment used are provided in the ESI (Sections S2 and S12).† Each of the materials underwent immediate amorphization after being exposed to atmospheric conditions after removal from oven at 160 °C, and for this reason we confirmed the stability of the materials by analyzing FT-IR spectra and SEM images after proton conductivity measurements (Fig. S28 and S44–S49†). Each impedance relationship corresponded closely to an $R_1 + Q_2/R_2 + Q_3$ equivalent circuit. In this model, R_1 represents the external (system) resistance, Q_2 is a constant phase element (CPE) describing non-ideal bulk dielectric behavior, R_2 corresponds to the sample resistance associated with proton conduction, and Q_3 denotes a CPE related to electrode polarization at the blocking electrode. This circuit is illustrated in the inset of Fig. 4a, which also presents a representative Nyquist plot for HIm@Zr-MOF samples (a summary for all materials is provided in Fig. S60†). The experimental results were fitted to a theoretical model based on the proposed equivalent circuit, serving as the foundation for all further analyses, with additional details available in the ESI (Section 12, Fig. S62–S65 and Table S7†). Imidazole-free samples (*e.g.*, UiO-68(TZ@Me) and UiO-68(TZndc@Me)) showed conductivity below detection limits, contrasting with the considerable conductivity of imidazole-containing samples (Fig. 4b). The HIm@UiO-68(TZ@Me) sample (0.72 μS cm^{-1}) shows the lowest conductivity, which we attributed to the presence of structural defects that introduce labile acidic OH and H_2O groups at zirconium nodes, a common feature of Zr-MOFs.[55,56] While these defective sites should be present in low concentrations across all tested samples, their contribution is expected to be uniform and remains secondary to the effect of carboxyl group functionalization. The introduction of COOH pendant groups was intended to increase the concentration of protonated imidazole carriers (H_2Im^+), and the highest conductivity was observed for HIm@UiO-68(Me@TZndc) (5.0 μS cm^{-1}). This value indicates relatively good conductivity under anhydrous conditions.

While conductivity depends on both carrier concentration and mobility, our materials were specifically designed to isolate conduction mechanism effects. The dominant proton carriers are H_2Im^+ species, whose concentration is influenced by both the anchored COOH group and adsorbed imidazole concentration. However, since both are weak Brønsted acids/bases, their interaction does not lead to a linear relationship between their concentration and the overall conductivity. The differences in conductivity between samples remain small (less than one order of magnitude), enabling us to focus on the activation energy as a reliable indicator of the proton transport mechanism, rather than the absolute quantity of transported charge.

The determination of activation energy using Arrhenius plots (Fig. 4c, S68 and Table S9†) for each sample sheds light on the dominant conduction mechanism. The results (Fig. 4d) indicate that none of these samples exhibit a pure Grotthuss mechanism, which generally requires a high carrier protonation degree or smaller pores to suppress diffusion.[57] HIm@UiO-

This journal is © The Royal Society of Chemistry 2025

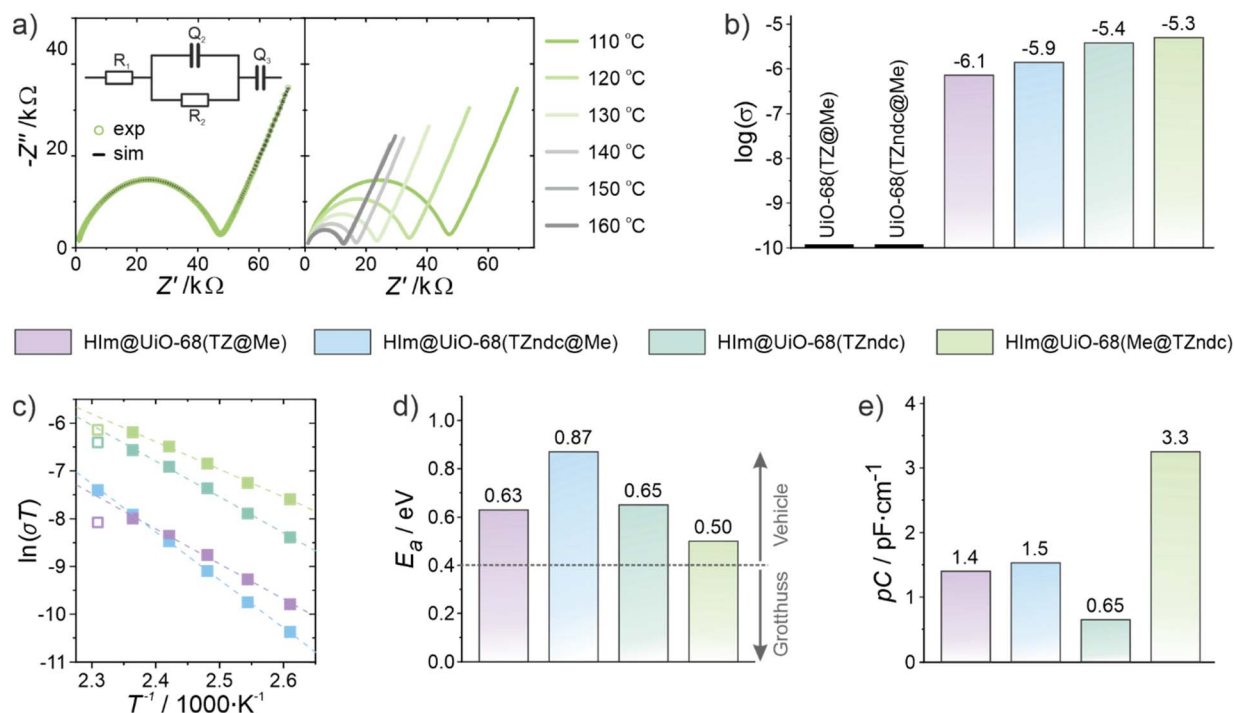*J. Mater. Chem. A*, 2025, **13**, 23671–23679 | **23675**

Fig. 4 Proton conduction studies: (a) Nyquist plots for HIm@UiO-68(Me@TZndc): experimental (black line) and simulated (green circles) data at 110 °C, fitting was based on the $R_1 + Q_2/R_2 + Q_3$ equivalent circuit (left part); and experimental curves at various temperatures (110–160 °C, right part). (b) Calculated conductivity values (σ) on a logarithmic scale for the materials with adsorbed imidazole (HIm@Zr-MOF) compared to the non-imidazole core–shell MOFs (first two bars). (c) Arrhenius plots for the HIm@Zr-MOF materials, empty symbols indicate points for the highest temperatures, deviating from the linear trend, not included in the determination of curve slopes. (d) Values of activation energy (E_a) of proton conduction determined from Arrhenius relationships, dashed line marks the arbitrary limit between two distinct conduction mechanisms. (e) Specific pseudocapacitance (pC) values determined by data fitting to an identical equivalent circuit.

68(Me@TZndc), with the lowest activation energy (0.50 eV), features a maximum H_2Im^+ concentration localized within the crystallite shell, whereas HIm@UiO-68(TZndc@Me), with the highest activation energy (0.86 eV), has H_2Im^+ ions concentrated in the crystallite core. Since the activation energy reflects the rate-limiting step in conduction, these findings align with the proposed conduction mechanism (Fig. 1). In HIm@UiO-68(TZndc@Me), macroscopic conduction relies on H_2Im^+ transport through a shell that lacks carboxylates, thus favoring a vehicle mechanism. In contrast, HIm@UiO-68(Me@TZndc) exhibits contributions from both the Grotthuss and the vehicle mechanism, as conduction occurs both through the shell and between neighboring crystallite shells. Both HIm@UiO-68(TZ@Me) and HIm@UiO-68(TZndc), with more uniformly distributed defects or carboxyl groups, act as intermediate cases (Fig. 1). Neither of them requires diffusion through the less favorable shell, allowing hydrogen-bonding networks to form throughout the sample volume. The relatively low H_2Im^+ concentration in these samples favors the vehicle mechanism; however, unlike HIm@UiO-68(Me@TZndc), charge carriers are dispersed also within the crystallite core, not only within the shell.

Close examination of Arrhenius plots reveals points corresponding to the highest temperatures (i.e. above 150 °C), that deviate from the linear trend (marked as empty symbols in Fig. 4c). This deviation is absent only for UiO-68(TZndc@Me),

suggesting that above 150 °C, imidazole, the charge carrier, leaks from the material, leading to a reduction in conductivity. For UiO-68(TZndc@Me), the increased concentration of HIm within the crystallite core allows the shell to act as a protective barrier. For all other materials, conduction through or between shells (grain-surface or inter-grain conduction) contributes significantly to global conductivity, and the loss of imidazole at the highest temperatures (160 °C) is reflected in a decline in conductivity.

Impedance measurements and related Nyquist plots were also used to estimate specific pseudocapacitance (pC) for each equivalent circuit, with values between 0.5–5 pF cm^{-1} across HIm@Zr-MOF samples (Fig. 4e). Literature data indicated that the pC value helps determine the conduction pathway (i.e. bulk vs. surface).[57] HIm@UiO-68(TZndc) exhibited the lowest pC (0.65 pF cm^{-1}), which is consistent with a homogeneous distribution of carboxyl groups and bulk-like conductivity similar to that of a uniform solid, in which inter-grain conduction is hardly significant. The highest pC value (3.3 pF cm^{-1}) in HIm@UiO-68(Me@TZndc) suggests significant surface conduction, consistent with its COOH group distribution in crystallite shells along grain boundaries. The inter-grain conduction has the highest significance for UiO-68(TZndc@Me), as manifested by the highest conduction activation energy. In addition, since the charge transport in UiO-68(TZndc@Me) occurs between the cores of neighbouring

23676 | J. Mater. Chem. A, 2025, **13**, 23671–23679

This journal is © The Royal Society of Chemistry 2025

crystallites (through acid-poor shells), surface conduction has a smaller contribution, *i.e.* pC = 1.5 pF cm^{-1} is smaller than for HIm@UiO-68(Me@TZndc), with acid-rich shells (pC = 3.3 pF cm^{-1}).

Conclusion

We have prepared spatially separated acid sites in two swappable zirconium MOF-based core–shell systems, based on two sequential strategies of controlled linker exchange and mild covalent modifications, to probe the mechanisms of proton conduction in polycrystalline samples. The resulting series of model hierarchical structures were functionalized with imidazole molecules to create humidity-independent pathways for proton transport. These pathways included incorporated acid sites that were located exclusively in the shells, in the cores or in the whole crystallites. Impedance measurements provided key parameters for the materials studied, including proton conductivities, activation energies and pseudocapacitances, confirming the significant role of external surface conduction in polycrystalline MOFs. Our work broadens the understanding of conduction in polycrystalline samples and provides a promising strategy for studying charge transport mechanisms in porous systems using hierarchical core–shell structures.

Experimental section

All necessary information on the materials, methods of synthesizing ligands and MOFs, modification methods as well as descriptions of the physicochemical examination techniques used can be found in ESI.†

Synthesis of MOFs and precursors

All reagents and solvents used for the syntheses of ligands, dienophiles and MOFs (unless otherwise noted) were commercially available and used without additional purification. ncn dienophile, H$_2$TZDC and H$_2$TPDC-Me linker precursors were synthesized using optimized literature protocols (see ESI, Section S3†). The synthesis of UiO-68(TZ) and UiO-68(Me) was performed following literature protocols[34,37] (see ESI, Section S3.2†). Protocols developed for the preparation of core–shell MOFs through solvent-assisted linker exchange (SALE) and covalent modification of tetrazine-based MOFs *via* the inverse electron-demand Diels–Alder (iEDDA) reaction are described in detail in ESI (Section S3.3).† The procedure for low-pressure imidazole adsorption was based on our previous work[6] (ESI, Section S3.4†).

Physicochemical characterization and GCMC simulations

Details for instrumentation used in this work are provided in the ESI (Section S2).† Structural characterization of synthesized precursors was performed by nuclear magnetic resonance (^{1}H NMR, Section S5†) and infrared vibrational spectroscopy (IR, Section S6†). Physicochemical characterization of MOFs was performed by powder X-ray diffraction (PXRD, Section S4†), ^{1}H NMR after digestion in a mixture of DMSO-d$_6$/D$_2$SO$_4$ (Section S5†), IR spectroscopy (Section S6†), dinitrogen volumetric adsorption analysis (at 77 K, Section S7†), scanning electron microscopy (SEM, Section S8†) and thermogravimetric analysis (TGA, Section S9†).

Theoretical N$_2$ sorption isotherms (at 77 K) and imidazole loadings (at 298 K and 393 K) in UiO-68(x) series were computed in grand canonical Monte Carlo (GCMC) simulations using the RASPA2 software.[58] The description of the used models and simulation details are described in ESI (Section S10).†

Direct analysis of ligand distribution for the model material UiO-68(TZ@Me) was performed with a scanning transmission X-ray microscope (STXM) utilizing synchrotron radiation (ESI, Section S11†) and aXis2000 software.[59]

Proton conduction was examined using Electrochemical Impedance Spectroscopy (EIS) in a four-electrode setup under constant pressure (4.5–5 MPa) and temperatures of 110–160 °C. The detailed assembly of the measurement cell is described in the ESI (Section S2 and Fig. S2).† For each measurement, the imaginary *versus* real impedance was measured across a frequency range of 4 Hz to 5 MHz, and EC-Lab software was used to fit the most suitable equivalent circuit, yielding the circuit resistance associated with ionic conduction (see ESI, Section S12† for details).

Data availability

The data supporting this article have been included as part of the ESI† and are deposited in the Repository of Open Research Data at https://uj.rodbuk.pl/ (https://doi.org/10.57903/UJ/NGRICH).

Author contributions

Damian Jędrzejowski: conceptualization: supporting; data curation: lead; formal analysis: lead; funding acquisition: supporting; investigation: lead; visualization: lead; writing – original draft: lead. Marzena Pander: conceptualization: supporting; data curation: lead; formal analysis: lead; investigation: lead; visualization: lead; writing – original draft: lead. Emilian Stachura: investigation: supporting. Krzysztof Matlak: data curation: supporting; methodology: supporting. Wojciech Bury: conceptualization: lead; funding acquisition: supporting; resources: lead; supervision: lead; writing – original draft: supporting; writing – review & editing: lead. Dariusz Matoga: conceptualization: lead; funding acquisition: supporting; resources: lead; supervision: lead; writing – original draft: supporting; writing – review & editing: lead.

Conflicts of interest

There are no conflicts to declare.

Acknowledgements

This journal is © The Royal Society of Chemistry 2025

J. Mater. Chem. A, 2025, 13, 23671–23679 | 23677

References

1 H. Furukawa, K. E. Cordova, M. O'Keeffe and O. M. Yaghi, *Science*, 2013, **341**, 1230444.

2 O. M. Yaghi, M. J. Kalmutzki and C. S. Diercks, *Introduction to Reticular Chemistry: Metal–Organic Frameworks and Covalent Organic Frameworks*, Wiley, Weinheim, 1st edn, 2019, DOI: 10.1002/9783527821099.

3 M. Yoon, K. Suh, S. Natarajan and K. Kim, *Angew. Chem., Int. Ed.*, 2013, **52**, 2688–2700.

4 X. Meng, H.-N. Wang, S.-Y. Song and H.-J. Zhang, *Chem. Soc. Rev.*, 2017, **46**, 464–480.

5 P. Ramaswamy, R. Matsuda, W. Kosaka, G. Akiyama, H. J. Jeon and S. Kitagawa, *Chem. Commun.*, 2013, **50**, 1144–1146.

6 M. Szufla, A. Choroś, W. Nitek and D. Matoga, *Chem.–Eur. J.*, 2022, **28**, e202200835.

7 M. Lupa, P. Kozyra, G. Jajko and D. Matoga, *ACS Appl. Mater. Interfaces*, 2021, **13**, 29820–29826.

8 D.-W. Lim and H. Kitagawa, *Chem. Rev.*, 2020, **120**, 8416–8467.

9 D. D. Borges, S. Devautour-Vinot, H. Jobic, J. Ollivier, F. Nouar, R. Semino, T. Devic, C. Serre, F. Paesani and G. Maurin, *Angew. Chem., Int. Ed.*, 2016, **55**, 3919–3924.

10 K. Zhang, G.-H. Wen, S.-S. Bao, L.-Q. Wu and J.-G. Jia, *ACS Appl. Energy Mater.*, 2020, **3**, 8198–8204.

11 S. Tominaka and A. K. Cheetham, *RSC Adv.*, 2014, **4**, 54382–54387.

12 H. Furukawa, U. Müller and O. M. Yaghi, *Angew. Chem., Int. Ed.*, 2015, **54**, 3417–3430.

13 L. Feng, S. Yuan, J.-L. Li, K.-Y. Wang, G. S. Day, P. Zhang, Y. Wang and H.-C. Zhou, *ACS Cent. Sci.*, 2018, **4**, 1719–1726.

14 T. Li, Y. Pan, K.-V. Peinemann and Z. Lai, *J. Membr. Sci.*, 2013, **425–426**, 235–242.

15 M. Kim, M. Pander and H. R. Moon, *ACS Appl. Electron. Mater.*, 2024, **6**, 3024–3038.

16 D. H. Hong, H. S. Shim, J. Ha and H. R. Moon, *Bull. Korean Chem. Soc.*, 2021, **42**, 956–969.

17 A. Helal, Z. H. Yamani, K. E. Cordova and O. M. Yaghi, *Natl. Sci. Rev.*, 2017, **4**, 296–298.

18 Z. Li, X.-B. Li, M. E. Light, A. E. Carrillo, A. Arauzo, M. Valvidares, C. Roscini, F. Teixidor, C. Viñas, F. Gándara, E. Bartolomé and J. G. Planas, *Adv. Funct. Mater.*, 2023, **33**, 2307369.

19 H. Deng, C. J. Doonan, H. Furukawa, R. B. Ferreira, J. Towne, C. B. Knobler, B. Wang and O. M. Yaghi, *Science*, 2010, **327**, 846–850.

20 X. Kong, H. Deng, F. Yan, J. Kim, J. A. Swisher, B. Smit, O. M. Yaghi and J. A. Reimer, *Science*, 2013, **341**, 882–885.

21 S. Jeong, J. Seong, S. W. Moon, J. Lim, S. B. Baek, S. K. Min and M. S. Lah, *Nat. Commun.*, 2022, **13**, 1027.

22 M. Kalaj, K. C. Bentz, S. Jr. Ayala, J. M. Palomba, K. S. Barcus, Y. Katayama and S. M. Cohen, *Chem. Rev.*, 2020, **120**, 8267–8302.

23 J. Xu, Y. Peng, W. Xing, Z. Ding, S. Zhang and H. Pang, *J. Energy Storage*, 2022, **53**, 105104.

24 S. Subudhi, S. P. Tripathy and K. Parida, *Inorg. Chem. Front.*, 2021, **8**, 1619–1636.

25 C. Liu, J. Wang, J. Wan and C. Yu, *Coord. Chem. Rev.*, 2021, **432**, 213743.

26 L. Chen, H.-F. Wang, C. Li and Q. Xu, *Chem. Sci.*, 2020, **11**, 5369–5403.

27 Q. Xia, Z. Li, C. Tan, Y. Liu, W. Gong and Y. Cui, *J. Am. Chem. Soc.*, 2017, **139**, 8259–8266.

28 O. Kwon, J. Y. Kim, S. Park, J. H. Lee, J. Ha, H. Park, H. R. Moon and J. Kim, *Nat. Commun.*, 2019, **10**, 3620.

29 L. Chai, J. Pan, Y. Hu, J. Qian and M. Hong, *Small*, 2021, **17**, 2100607.

30 K. C. Jayachandrababu, D. S. Sholl and S. Nair, *J. Am. Chem. Soc.*, 2017, **139**, 5906–5915.

31 J. A. Boissonnault, A. G. Wong-Foy and A. J. Matzger, *J. Am. Chem. Soc.*, 2017, **139**, 14841–14844.

32 H. Jiang, Q. Gong, R. Zhang and H. Yuan, *Coord. Chem. Rev.*, 2024, **499**, 215501.

33 G. Gómez-Tenés, P. Gimeno-Fonquernie, A. Misturini, C. Chinchilla-Garzón, V. Carratalá, L. Cisneros and C. Martí-Gastaldo, *Chem. Commun.*, 2024, **60**, 12977–12985.

34 B. Lerma-Berlanga, C. R. Ganivet, N. Almora-Barrios, S. Tatay, Y. Peng, J. Albero, O. Fabelo, J. González-Platas, H. García, N. M. Padial and C. Martí-Gastaldo, *J. Am. Chem. Soc.*, 2021, **143**, 1798–1806.

35 O. Karagiaridi, W. Bury, E. Tylianakis, A. A. Sarjeant, J. T. Hupp and O. K. Farha, *Chem. Mater.*, 2013, **25**, 3499–3503.

36 J. H. Cavka, S. Jakobsen, U. Olsbye, N. Guillou, C. Lamberti, S. Bordiga and K. P. Lillerud, *J. Am. Chem. Soc.*, 2008, **130**, 13850–13851.

37 H.-L. Jiang, D. Feng, T.-F. Liu, J.-R. Li and H.-C. Zhou, *J. Am. Chem. Soc.*, 2012, **134**, 14690–14693.

38 A. Centrone, B. Lerma-Berlanga, A. J. Biacchi, C. Fernández-Conde, G. Pavlidis and C. Marti-Gastaldo, *Adv. Funct. Mater.*, 2023, **33**, 2302357.

39 S. Mayer and K. Lang, *Synthesis*, 2017, **49**, 830–848.

23678 | *J. Mater. Chem. A*, 2025, **13**, 23671–23679

This journal is © The Royal Society of Chemistry 2025

40 B. L. Oliveira, Z. Guo and G. J. L. Bernardes, *Chem. Soc. Rev.*, 2017, **46**, 4895–4950.

41 M. Kalaj and S. M. Cohen, *ACS Cent. Sci.*, 2020, **6**, 1046–1057.

42 T. Islamoglu, S. Goswami, Z. Li, A. J. Howarth, O. K. Farha and J. T. Hupp, *Acc. Chem. Res.*, 2017, **50**, 805–813.

43 Y.-J. Zhang, H.-X. Nie, M.-H. Yu and Z. Chang, *J. Solid State Chem.France*, 2021, **300**, 122257.

44 L. Feng, S.-H. Lo, K. Tan, B.-H. Li, S. Yuan, Y.-F. Lin, C.-H. Lin, S.-L. Wang, K.-L. Lu and H.-C. Zhou, *Matter*, 2020, **2**, 988–999.

45 J. E. Clements, J. R. Price, S. M. Neville and C. J. Kepert, *Angew. Chem., Int. Ed.*, 2014, **53**, 10164–10168.

46 C. Chen, C. A. Allen and S. M. Cohen, *Inorg. Chem.*, 2011, **50**, 10534–10536.

47 D. Jędrzejowski, M. Pander, W. Nitek, W. Bury and D. Matoga, *Chem. Mater.*, 2021, **33**, 7509–7517.

48 D. Jędrzejowski, M. Ryndak, J. J. Zakrzewski, M. Hodorowicz, S. Chorazy and D. Matoga, *ACS Appl. Mater. Interfaces*, 2023, **15**, 25661–25670.

49 B. Lerma-Berlanga, N. M. Padial, M. Galbiati, I. Brotons-Alcázar, J. Albero, H. García, A. Forment-Aliaga, C. R. Ganivet and C. Martí-Gastaldo, *Adv. Funct. Mater.*, 2023, **33**, 2302246.

50 B. Lerma-Berlanga, C. R. Ganivet, N. Almora-Barrios, R. Vismara, J. A. R. Navarro, S. Tatay, N. M. Padial and C. Martí-Gastaldo, *Angew. Chem., Int. Ed.*, 2022, **61**, e202208139.

51 M. Casciola, G. Alberti, M. Sganappa and R. Narducci, *J. Power Sources*, 2006, **162**, 141–145.

52 G. Zhang, G. Yang, S. Li, Q. Shen, H. Wang, Z. Li, Y. Zhou and W. Ye, *Membranes*, 2021, **11**, 695.

53 F.-M. Zhang, L.-Z. Dong, J.-S. Qin, W. Guan, J. Liu, S.-L. Li, M. Lu, Y.-Q. Lan, Z.-M. Su and H.-C. Zhou, *J. Am. Chem. Soc.*, 2017, **139**, 6183–6189.

54 H.-B. Luo, Q. Ren, P. Wang, J. Zhang, L. Wang and X.-M. Ren, *ACS Appl. Mater. Interfaces*, 2019, **11**, 9164–9171.

55 M. Szufla, J. A. R. Navarro, K. Góra-Marek and D. Matoga, *ACS Appl. Mater. Interfaces*, 2023, **15**, 28184–28192.

56 O. V. Gutov, M. G. Hevia, E. C. Escudero-Adán and A. Shafir, *Inorg. Chem.*, 2015, **54**, 8396–8400.

57 J. T. S. Irvine, D. C. Sinclair and A. R. West, *Adv. Mater.*, 1990, **2**, 132–138.

58 D. Dubbeldam, S. Calero, D. E. Ellis and R. Q. Snurr, *Mol. Simul.*, 2016, **42**, 81–101.

59 A. P. Hitchcock, *J. Electron Spectrosc. Relat. Phenom.*, 2023, **266**, 147360.

This journal is © The Royal Society of Chemistry 2025

J. Mater. Chem. A, 2025, **13**, 23671–23679 | **23679**